Experimental investigations of internal and effective stresses during fatigue loading of high-strength steel
Etude expérimentale des contraintes internes et effectives dans un acier à haute résistance sollicité en fatigue

Flavien Vucko, Cédric Bosch, David Delafosse

Ecole Nationale Supérieure des Mines, SMS-EMSE, CNRS:UMR5307,

LGF:LaboratoireGeorgesFriedel, 158coursFauriel, 42023 Saint-Etienne, France

Résumé

Des essais de fatigue oligocyclique ont été effectués à différentes amplitudes de déformation plastique et à température ambiante, sur un acier à haute résistance, martensitique trempé et revenu. Les composantes internes et effectives de la contrainte d'écoulement ont été analysées par la méthode de Handfield et Dickson. La contrainte interne est affectée par l'amplitude de déformation plastique. Au contraire, l'évolution de la composante athermique de la contrainte effective est indépendante de cette amplitude. La composante thermiquement activée augmente avec l'amplitude de déformation plastique mais reste constante en fonction de la déformation plastique cumulée. Les évolutions microstructurales dans le matériau déformé en fatigue ont été étudiées par microscopie électronique à transmission et par diffraction de rayons X. Les évolutions des contraintes internes et effectives sont alors discutées en fonction de ces observations.

Abstract

Low cycle fatigue tests are performed on a high strength tempered martensitic steel at different plastic strain amplitudes at room temperature. Internal and effective components of the flow stress are analyzed using Handfield and Dickson's method. The internal stress is affected by the plastic strain amplitude. Conversely, the evolution of the athermal component of the effective stress with the number of cycles is independent of the plastic strain amplitude. The thermal part of the effective stress increases with the plastic strain amplitude, but remains constant with plastic strain accumulation. Microstructural changes in the cyclically deformed material are investigated by means of transmission electronic mycroscopy and X-Ray characterizations. Internal and effective stress evolutions are discussed based on these observations.

Table of content

I. Introduction

The fatigue lifetime of materials is mainly controlled by initiation of a crack from microstructural or surface defects [1]. Without pre-existent critical defects, as porosity or coarse precipitates, initiation is induced by emergent persistent slip bands (PSB) or dislocation cells, depending on materials composition and crystallography [1]. The rearrangement of dislocations is directly linked to strain and stress state in the material. The aim of this study is to use a mechanical approach which could be correlated to the evolution of the microstructure leading to the crack initiation.

The cyclic behavior of high-strength steel is characterized by the shape and the evolution of the cyclic stress-strain hysteresis loops [2–9]. At room temperature, the cyclic plastic strain is fully controlled by the mobility and the arrangement of dislocations [10], [11]. Following Cottrell's analysis [2], the resolved shear stress experienced by dislocations during cyclic straining split in two components: the internal (X) and the effective (Σ_{ef}) stress. The former is related to long-range interactions between dislocations and obstacles and to local strain incompatibilities. The latter is due to short-range interactions. The effective stress is partially affected by thermal activation. As such, it can be further decomposed into two additive components Σ^* and $\Sigma\mu$ which are respectively the thermally activated part and the athermal part of the effective stress. In order to evaluate these components of the uniaxial flow stress, methods based on relaxation tests [12], [13], strain rate or temperature change tests [14], [15], successive discharges [16] and hysteresis loop analysis [3–5] have been developed.

Handfield and Dickson [5] analyzed the hysteresis loops based on Cottrell's framework to separate the effective and internal components of the stress. This method is applied on the high-strength steel S690QL (EN 10137-2) which is quenched-tempered martensitic steel. Low-cycle fatigue (LCF) tests are performed at room temperature and each cycle is analyzed. Results are discussed using additional techniques such as transmission electron microscopy (TEM), X-Ray diffraction and tensile tests at different temperatures [17–19].

II. Material and experimental procedure

II.1. Material

The material of the study is a high strength steel S690QL (EN 10137-2). It exhibits a tempered martensitic microstructure consisting of laths of about 200 nm width. Laths are gathered in blocks and packets which are contained in prior austenite grain with a cluster size ranging from

10 to 20 μm. The steel chemical composition is given in table 1. Tempering consisted in two hours at 550 °C after austenitization at 920 °C and water quenching. No retained austenite was revealed by X-ray analysis. The mechanical properties are shown in table 2.

Table 1: Chemical composition of steel S690QL (weight %)

Elements	C	Si	Mn	Mo	Nb	Ni	Ti	S
wt.%	0.16	0.33	1.22	0.25	≤0.10	0.11	≤0.05	≤0.001
Elements	P	V	Zr	N	B	Cr	Cu	Fe
wt.%	≤0.02	≤0.1	≤0.1	≤0.015	≤0.005	0.29	≤0.1	Bal.

Table 2: Mechanical properties of steel S690QL at room temperature

	YS (MPa) at $\varepsilon p = 0.2$ %	UTS (MPa)	Elongation (%)
Steel S690QL	726	*940*	*35*

II.2. Low cycle fatigue tests

LCF tests controlled by plastic strain are carried out at a plastic strain rate $d\varepsilon_p/dt = 5.10^{-4}$ s^{-1} and plastic strain amplitudes between $\Delta\varepsilon_p/2 = +/-0.2$ % and $+/-1$ %. They are conducted with a control waveform triangular and symmetrical (i.e.: constant plastic strain rate and load ratio equal to -1). Cylindrical specimens with a 10 mm gauge length and 8 mm diameter are used. Strain is controlled by an extensometer of 7 mm $+/-1$ mm gauge length. A cross-compensation is applied to the extensometer signal to cancel the elastic strain.

II.3. Hysteresis loop analysis

Each hysteresis cycle is analyzed using Handfield and Dickson's method (Fig.1). Frontiers of the elastic domain ($\sigma_{e\,max}$ and $\sigma_{e\,min}$) are determined with a plastic strain offset of 5.10^{-5}. This offset is chosen to match with the sensitivity of the extensometer and is the same for all plastic strain amplitudes. Increasing the offset leads to increase the estimated value of the athermal component of the effective stress and decrease the thermal part, but the estimated internal stress is not affected. The internal stress X, the thermal effective stress Σ^* and the athermal effective stress Σ_μ are calculated with equations summarized in table 3.

Table 3: Internal stress, thermal and athermal effective stress equations (symbols of defined in figure 2)

$$X = \frac{\sigma_{e\,max} + \sigma_{e\,min}}{2} \qquad \Sigma_\mu = \frac{\sigma_{e\,max} - \sigma_{e\,min}}{2} \qquad \Sigma^* = \sigma_{max} - \sigma_{e\,max}$$
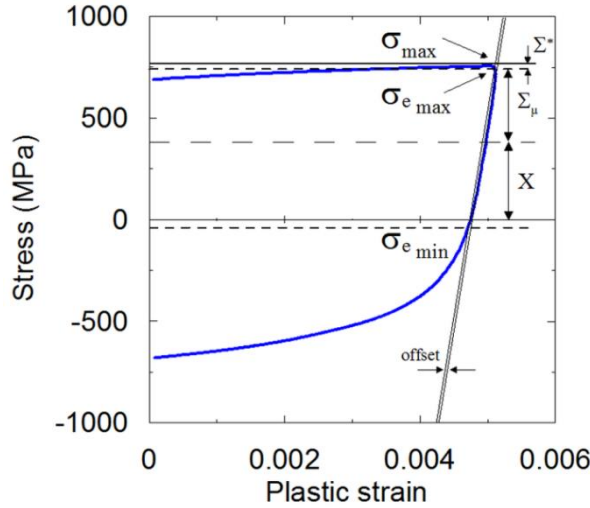

Fig.1: Handfield and Dickson's method for hysteresis loop analysis

II.4. X-Ray diffraction

The dislocation density is investigated by X-Ray diffraction line profile analysis [20]. As presented in figure 2, peak broadening is influenced by the dislocation density. The momentum method [21–23] is applied to determine the dislocation density evolution during cyclic loading. The second and fourth restricted moments of the measured intensity distribution are linked to the dislocation density and the coherent domain size, as given by equations 1 and 2, respectively:

$$M_2(q) = \frac{1}{\pi^2 \varepsilon_F} q - \frac{L}{4\pi^2 K^2 \varepsilon_F{}^2} + \frac{\Lambda \langle \rho \rangle \ln(q/q_0)}{2\pi^2} \qquad \text{Eq.1}$$

$$\frac{M_4(q)}{q^2} = \frac{1}{3\pi^2 \varepsilon_F} q + \frac{\Lambda \langle \rho \rangle}{4\pi^2} + \frac{3\Lambda \langle \rho \rangle}{(2\pi)^4 q \varepsilon_F} \ln(q/q_1) + \frac{3\Lambda^2 \langle \rho^2 \rangle}{4\pi^4 q^2} \ln^2(q/q_2) \qquad \text{Eq.2}$$

with $q=2(sin(\theta)-sin(\theta_0))/\lambda$ and $\Lambda=\pi/2g^2b^2C$. θ and θ_0 are the diffraction and the Bragg angles. λ is the wavelength of the illuminating X-Ray. C is the contrast factor evaluated by texture analysis [21]. $<\rho>$ is the average dislocation density. g is the magnitude of the diffraction vector. b is the magnitude of the Burgers vector. ε_F is the coherent domain size. In equation 2, the third and fourth terms are negligible in our case since size broadening is the dominant contribution [23]. Data are recorded using a Panalytical MRD diffractometer with Co K_α radiation (1.790 Å) and optics equipped with a slit of 1/8°.
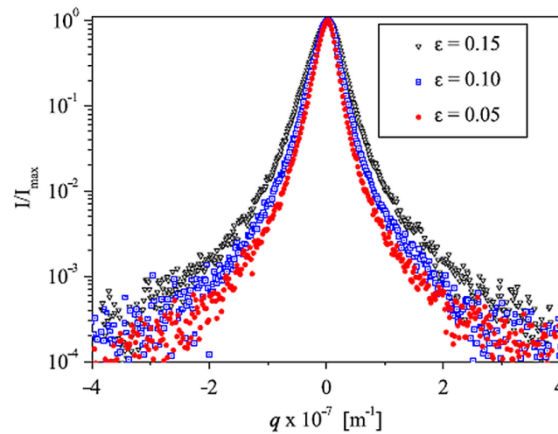

Fig.2: Lines profiles of plane strain compressed
Al-0.3%Mn single crystals, after Borbély [22]

II.5. Additional characterization

Microstructural investigation by TEM on fatigue specimens is performed using a PHILIPS FEI CM 200 microscope operating at 200 kV. Thin samples with a diameter of 3 mm and a thickness of 100 μm are machined from fatigue specimens by saw-wire cutting. Final thickness (< 200 nm) is obtained by electropolishing in a solution of 10%-perchloric acid and ethanol at 15 V for about 40 s.

The temperature-dependence of the macroscopic stress is studied with tensile tests at temperatures from 150 up to 420 K [14], [17–19]. Tests are performed at constant strain rate $d\varepsilon/dt=5.10^{-4}$ s^{-1}. Two series of experiments are carried out on specimens with or without cyclic pre-hardening, which consists in cycling at constant plastic strain amplitude $\Delta\varepsilon_p/2 = +/-0.5$ % and constant plastic strain rate $d\varepsilon_p/dt=5.10^{-4}$ s^{-1} for 120 cycles.

III. Results

III.1. Cyclic stress evolution

An example LCF test at a plastic strain amplitude $\Delta\varepsilon_p/2 = 0.5\%$ is given in figure 3a. The evolution of the half stress amplitude with cycle number is presented in figure 3b. The cumulative plastic strain p, for a LCF tests, is defined by $p = 2 \times N \times \Delta\varepsilon_p$, with N the number of cycles and $\Delta\varepsilon_p$ the plastic strain amplitude for each cycle. The stress amplitude is an increasing function of the applied strain amplitude. The evolution of the stress amplitude is qualitatively comparable across all investigated strain amplitudes: the steel exhibits a cyclic softening down to linear regime.
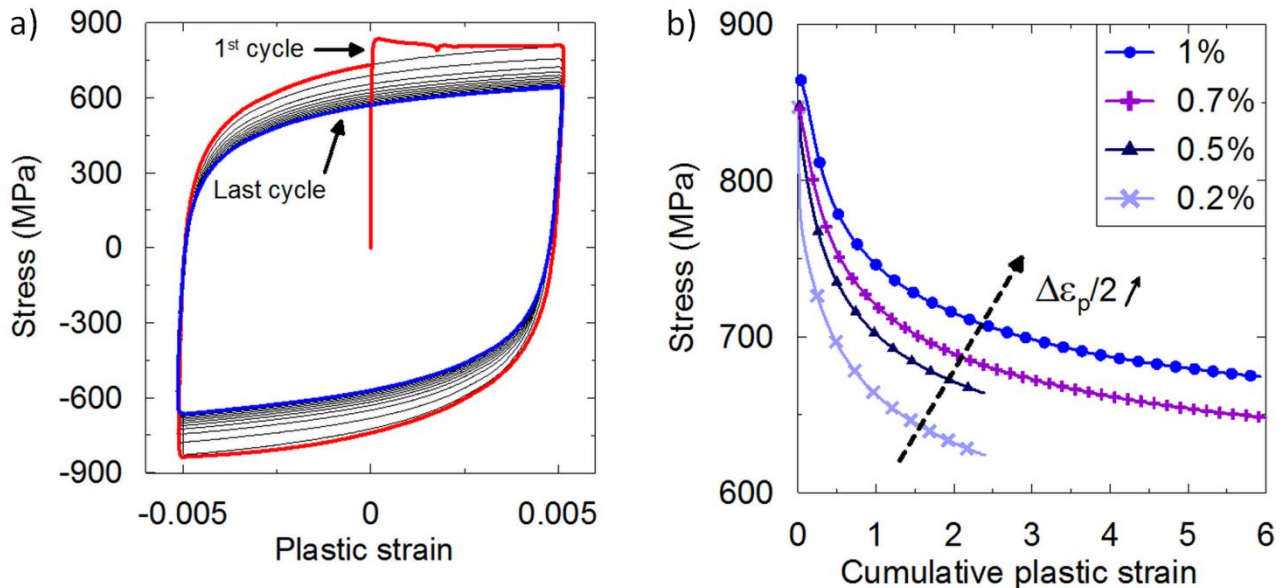

Fig.3: (a) example of hysteresis loops at a plastic strain amplitude $\Delta\varepsilon_p/2 = +/-0.5\%$ and (b) evolution of the half stress amplitude with cumulative plastic strain for imposed plastic strain amplitudes between $\Delta\varepsilon_p/2 = 0.2\%$ and 1%

The effective stress is divided into a thermally activated component Σ^* and an athermal component Σ_μ. Their evolutions are presented in figure 4. The thermally activated part of the effective stress is greater when the applied strain amplitude is increased, but does not evolve with the number of cycles.
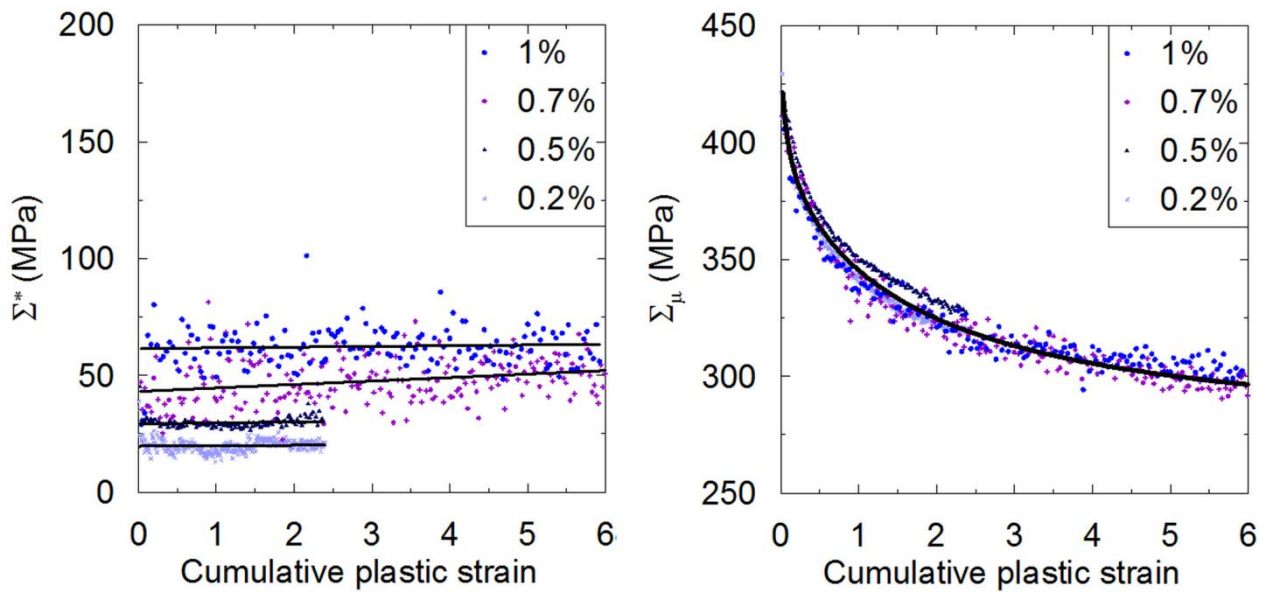
Fig.4: Evolution of the thermal (left) and athermal (right) components of the effective stress for plastic strain amplitudes between $\Delta\varepsilon_p/2 = 0.2\ \%$ and $1\ \%$

Conversely, the evolution of the athermal component is identical at all investigated plastic strain amplitudes. It exhibits a strong softening for $p < 2$ and then, a slower quasi-linear softening.

The internal stress is plotted in figure 5 as a function of the cumulative plastic strain. It increases with the applied strain amplitude. The evolution is similar across all strain amplitudes and consists in a steep softening for a cumulative plastic strain $p < 2$ and followed by a quasi-linear evolution at higher accumulated plastic strains.

8
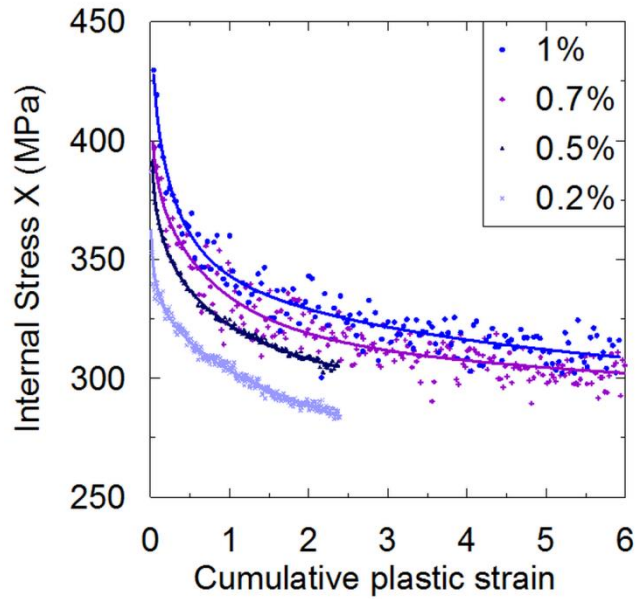
Fig.5: Evolution of the internal stress for plastic strain amplitudes between $\Delta\varepsilon_p/2 = 0.2$ % and 1 %
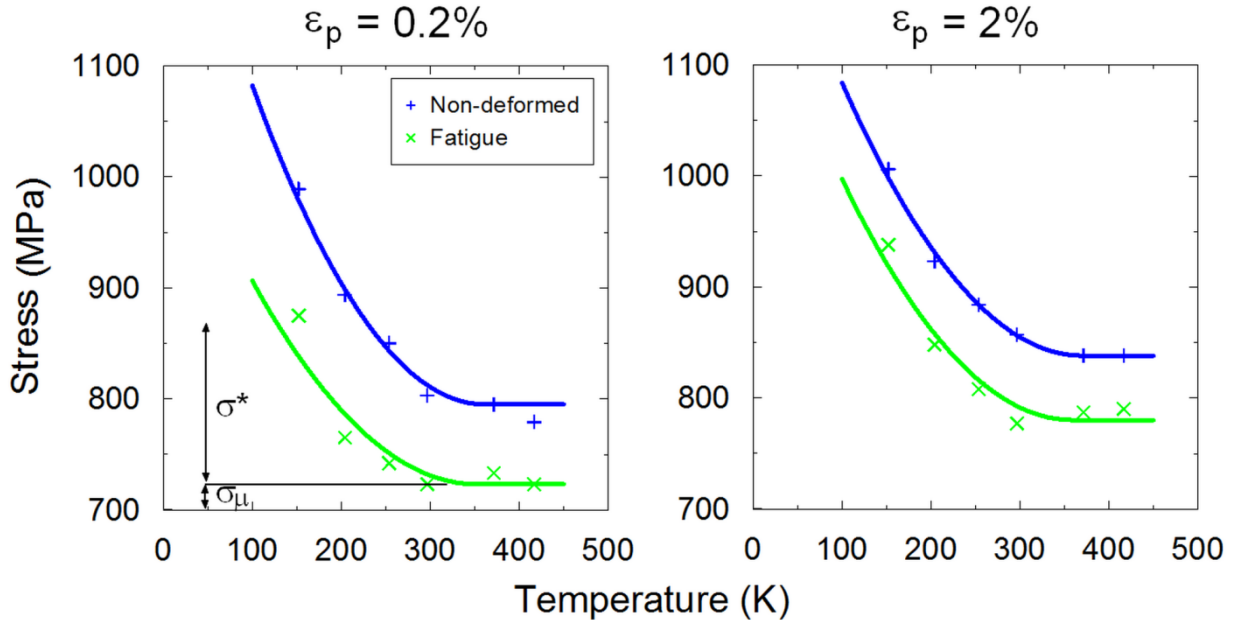
Fig.6: Temperature-dependence of the tensile flow stress at 0.2 % (left) and 2 % (right) plastic strain

The thermally activated part of the stress is measured by tensile tests at different temperatures. Values of the flow stress at 0.2% and 2% plastic strain for each temperature are reported in figure 6. As expected from the cyclic stress-strain data (Fig.3), the athermal part of the stress decreases

9

after cyclic prestraining (72 MPa at 0.2 % and 58 MPa at 2 %). At room temperature, the thermal part of the stress, σ^*, is not affected by cyclic pre-hardening.

III.2. Dislocation density

The momentum method to estimate the dislocation density is used for two peaks for each sample: (110) and (211). To accurately estimate the average dislocation density, the contrast factor has to be determined using texture analysis [21]. X-Ray analyses are performed on a normal-transverse plane; the rolling direction is perpendicular to the surface. Pole figures are centro-symmetric with a maximum intensity at 0° and 60° for (110) planes, 45° for (200) planes and 30° for (211) planes. These results show that [110] lies along the rolling direction. Schmid factors calculation show that only 4 systems are activated: (011) [11-1], (101) [11-1], (01-1) [111] and (10-1) [111]. For this calculation, {110} <111> systems only are considered. We assume no gliding along {211} <111> systems as observed in pure iron [24], [25] and confirmed by atomistic simulations in bcc tungsten [26]. {211} planes analyzed by X-Ray diffraction are (211), (121), (12-1) and (21-1) because they all have the same angle with [110], which is the smallest angle among all the {211} planes. The contrast factors of dislocations are calculated with iron contrast factors [21]. Results are summarized in table 4.

Table 4: Dislocations contrast factors of iron [20]

C	(110)	(211)	(121)	(12-1)	(21-1)
(011) [11-1]	0.2996	0.1057	0.198	0.2946	0.2505
(101) [11-1]	0.2996	0.198	0.1057	0.2505	0.2946
(01-1) [111]	0.2996	0.2505	0.2946	0.198	0.1057
(10-1) [111]	0.2996	0.2946	0.2505	0.1057	0.198
$\overline{C}$	0.2996	0.2122			

Dislocation densities in samples after monotonic and cyclic straining are presented in figure 7. These densities are the means of the results obtained from (110) and (211) diffraction peaks. Data scattering is represented by errors bars. The initial dislocation density is $7.2+/-0.6\times10^{14}$ m^{-2}. It is increases rapidly during tensile straining, reaching $2.0+/-0.1\times10^{15}$ m^{-2} at 6% and $2.1+/-0.1\times10^{15}$ m^{-2} at 10% of total deformation. During cyclic straining, the dislocation density initially

increases slightly during the first few cycles; at p = 0.04, $\varrho_{0.5\%}$ = 8.05+/-0.9×10^{14} m^{-2} and $\varrho_{0.2\%}$ = 7.6+/-0.8×10^{14} m^{-2} for plastic strain amplitudes $\Delta\varepsilon_p/2$ of 0.5 % and 0.2 % respectively. Then, the dislocation density decreases with the cumulative plastic strain. The decrease is comparable for both plastic strain amplitudes investigated; at p=2.4, ϱ = 5.7+/-0.7×10^{14} m^{-2}.
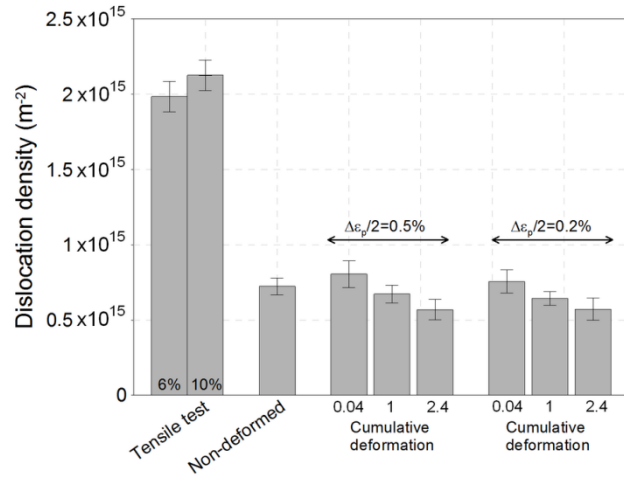
Fig.7: Dislocation density measured by momentum analysis of X-Ray line profiles, for tensile and cyclic straining, at two plastic strain amplitudes (+/- 0.2 and +/- 0.5%)

III.3. Dislocation cells

TEM observations are performed on non-deformed and cyclically deformed samples (120 cycles at constant plastic strain amplitude $\Delta\varepsilon_p/2$ = +/-0.5 % and constant plastic strain rate dε_p/dt = 5.10^{-4} s^{-1}). Dislocations cells are observed after cycling as shown in figure 8.

Fig.13: a) TEM observation of sample after cyclic straining (magnification 65000) and b) diffraction diagram

Many precipitates are also detected with TEM observations. Some small coherent precipitates, about 50 nm, are present inside martensite laths, and larger non coherent precipitates with a diameter of about 150 nm are located on lath and grain boundaries.

IV. Discussion

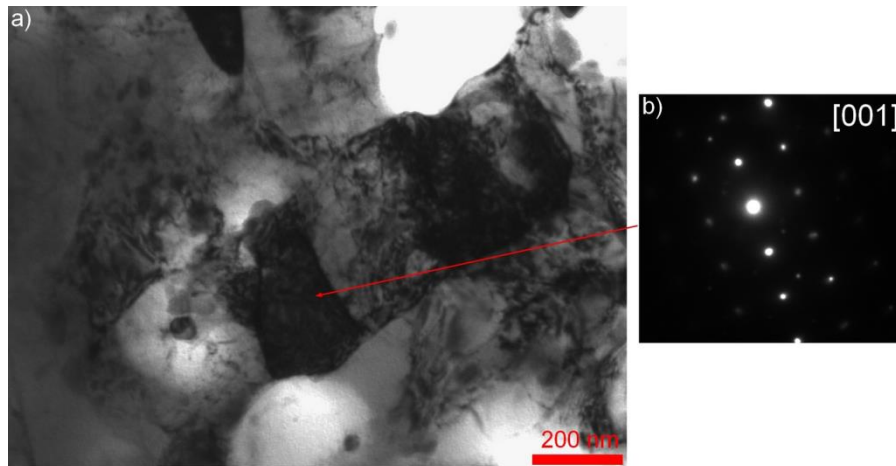The cyclic softening is achieved by a decrease of the athermal effective stress and internal stress for all investigated strain amplitudes. Conversely, the thermal part of the effective stress remains constant during the plastic stain accumulation. These different contributions to the flow stress are due to the interactions of mobile dislocation with microstructural obstacles [27]. The internal stress can be linked to interactions with long-range obstacles such as dislocation pile-ups, precipitates, dislocation walls, grain boundaries, and other local strain incompatibilities [28–31]. The athermal component of the effective stress results mainly from interactions with forest dislocations [32] and precipitate strengthening [33] (Orowan by-passing [34] or shearing mechanisms). Finally, the thermal part of the effective stress is caused by lattice friction [35–38], double-kink formation [39–41], edge dipole formation, cross-slip [42], [43] and solid solution interactions [44].

In the case of fatigue loading, the dislocation density decreases with plastic strain accumulation. Cyclic strain induces a rearrangement of dislocations in cells. These cells are formed in metals with medium and high stacking fault energies in order to reduce the elastic energy stored in the material and to accommodate more plastic strain [45]. To develop such patterns, dislocation

generation and annihilation processes have to operate. The cross-slip of screw dislocation is obviously a very important mechanism in the production of specific fatigue sub-structures [43], [46], [47]. Cross-slip allows screw dislocations of opposite sign gliding in neighboring parallel planes to meet and annihilate each other, leaving trailing edge dipole debris [42]. Their clustering results in the formation of cell walls. Consequently, cell formation by cyclic straining is accounts for both dislocation density decreases inside the cell and accumulation in cell walls, with possible recovery. It also reduces the size of coherent domain in crystals and so modifies the distribution of long range obstacles for gliding dislocations.

The internal stress increases with the plastic strain amplitude, which means that interactions are stronger at higher plastic stain level. Dislocation pile-ups are wiped out by cyclic straining, which decreases the internal stress. Recovery processes in cell walls also reduce this stress. The evolution of the cyclic softening with plastic strain is independent of the applied plastic strain amplitude within the investigated range, meaning that the controlling parameter is indeed the cumulative plastic strain provided to the material.

The decrease of the athermal effective stress can be related to the decrease of dislocation density inside cells. Forest interactions are reduced due to dislocation annihilation by cross-slip inside cells. The rate of decrease is identical at all investigated plastic strain amplitudes, meaning that generation and annihilation processes are mainly dependent of plastic strain accumulation. X-Ray diffraction results also show a comparable decrease for plastic strain amplitudes $\Delta\varepsilon_p/2$ of 0.5 % and 0.2 %. Finally, fatigue straining may lead to the dissolution by shearing of coherent precipitates inside martensite laths, which would also cause a decrease of the athermal effective stress.

Concerning the thermal part of the effective stress, all previously quoted mechanisms can be active. All of them are affected by the level of stress/strain. But, edge dipole formation and cross-slip are linked to the forest dislocation density. So lattice friction, double-kink formation and solid solution interactions may be the main mechanisms. For double-kink formation, as shown in figure 6, room temperature is close to athermal regime where edge and screw dislocations have the same mobility, so where the line tension mechanism prevails on the double-kink one.

Conclusion

A detailed analysis of the evolution of the cyclic stress, dislocation density and dislocation patterns were carried out in the complex nano-scale microstructure of a high strength tempered

martensitic steel. Internal and effective components of the stress were extracted from hysteresis cycles of low cycle fatigue tests at different strain amplitudes. Both the internal stress and the athermal part of the effective stress are dependent on the cumulative plastic strain, which is related to the mechanical energy provided to the material. The thermal part of the effective stress depends only on the applied strain amplitude.

Combined TEM observations and quantitative analysis of X-Ray diffraction peaks showed that cyclic softening is linked to microstructural modifications during cyclic straining. The decrease of the internal stress is due to cell formation and that of the athermal effective stress is caused by the reduction of dislocation density inside cells. Other mechanisms might operate, but the above two are the most consistent with TEM observations and X-Ray measurements performed in our material for the investigated cyclic strain amplitudes.

References

[1]   S. Suresh, Fatigue of Materials. Cambridge: University Press, 1991, p. 617.

[2]   A. H. Cottrell, Dislocations and plastic flow in crystals, Oxford Uni. London: , 1953.

[3]   D. Kuhlmann-Wilsdorf and C. Laird, "Dislocation Behavior in Fatigue," Materials Science and Engineering, vol. 27, pp. 137–156, 1977.

[4]   J. Polak, M. Klesnil, and J. Helesic, "The hysteresis loop. 2. Analysis of the loop shape," Fatigue & Fracture of Engineering Materials and Structures, vol. 5, no. 1, pp. 33–44, Jan. 1982.

[5]   J. I. Dickson, J. Boutin, and L. Handfield, "A comparison of two simple methods for measuring cyclic internal and effective stresses," Materials Science and Engineering, vol. 64, no. 1, pp. L7–L11, May 1984.

[6]   C. Guillemer-Neel, V. Bobet, and M. Clavel, "Cyclic deformation behaviour and Bauschinger effect in ductile cast iron," Materials Science and Engineering: A, vol. 272, no. 2, pp. 431–442, Nov. 1999.

[7]   J. Polák, F. Fardoun, and S. Degallaix, "Analysis of the hysteresis loop in stainless steels I. Austenitic and ferritic steels," Materials Science and Engineering: A, vol. 297, pp. 144–153, 2001.

[8]   C. Gaudin, C. Guillemer-Neel, and X. Feaugas, "Hardening rate under reverse loading in 316 L : Back stress and effective stress evolutions," Journal de physique. IV, vol. 11, no. PR5, pp. 285–292, 2001.

[9]   B. Fournier, M. Sauzay, C. Caës, M. Noblecourt, and M. Mottot, "Analysis of the hysteresis loops of a martensitic steel," Materials Science and Engineering: A, vol. 437, no. 2, pp. 183–196, Nov. 2006.

[10]   H.-F. Chai and C. Laird, "Mechanisms of cyclic softening and cyclic creep in low carbon steel," Materials Science and Engineering, vol. 93, pp. 159–174, Sep. 1987.

[11]   M. F. Giordana, P.-F. Giroux, I. Alvarez-Armas, M. Sauzay, a. Armas, and T. Kruml, "Microstructure evolution during cyclic tests on EUROFER 97 at room temperature. TEM observation and modelling," Materials Science and Engineering: A, vol. 550, pp. 103–111, Jul. 2012.

[12]   E. Krempl, "Relaxation behavior and modeling," International Journal of Plasticity, vol. 17, no. 10, pp. 1419–1436, Oct. 2001.

[13]   Z. Trojanová, K. Máthis, P. Lukáč, G. Németh, and F. Chmelík, "Internal stress and thermally activated dislocation motion in an AZ63 magnesium alloy," Materials Chemistry and Physics, vol. 130, no. 3, pp. 1146–1150, Nov. 2011.

[14]   F. A. Smidt, "An analysis of thermally activated flow in alpha iron based on T-tau* considerations," Acta Metallurgica, vol. 17, pp. 381–392, 1969.

[15]   P. Braillon, L. Kubin, and J. Serughetti, "Plastic deformation of calcite single crystals deformed in compression parallel to [111]," Physica Status Solidi (a), vol. 45, no. 2, pp. 453–462, Feb. 1978.

[16]   J. Polak, M. Klesnil, and J. Helesic, "The hysteresis loop. 3. Stress-dip experiment," Fatigue & Fracture of Engineering Materials and Structures, vol. 5, no. 1, pp. 45–56, Jan. 1982.

[17]   N. Brown and R. A. Ekvall, "Temperature dependence of the yield points in iron," Acta Metallurgica, vol. 10, pp. 1101–1107, 1962.

[18] P. Chomel and J. P. Cottu, "Influence of substitutional elements on flow stress in iron at low temperature," Acta Metallurgica, vol. 30, no. 8, pp. 1481–1491, Aug. 1982.

[19] L. Hollang, D. Brunner, and A. Seeger, "Work hardening and flow stress of ultrapure molybdenum single crystals," Materials Science and Engineering: A, vol. 319–321, pp. 233–236, Dec. 2001.

[20] P. Gay, P. . Hirsch, and A. Kelly, "The estimation of dislocation densities in metals from X-ray data," Acta Metallurgica, vol. 1, no. 3, pp. 315–319, May 1953.

[21] A. Borbély, J. H. Driver, and T. Ungár, "An X-ray method for the determination of stored energies in texture components of deformed metals; application to cold worked ultra high purity iron," Acta Materialia, vol. 48, no. 8, pp. 2005–2016, May 2000.

[22] A. Borbély, A. Révész, and I. Groma, "Momentum method applied to evaluation of size and strain in ball-milled iron," Zeitschrift für Kristallographie Supplements, vol. 2006, no. suppl_23_2006, pp. 87–92, Jun. 2006.

[23] A. Borbély and T. Ungár, "X-ray line profiles analysis of plastically deformed metals," Comptes Rendus Physique, vol. 13, no. 3, pp. 293–306, Apr. 2012.

[24] D. Caillard, "Kinetics of dislocations in pure Fe. Part I. In situ straining experiments at room temperature," Acta Materialia, vol. 58, no. 9, pp. 3493–3503, May 2010.

[25] D. Caillard, "Kinetics of dislocations in pure Fe. Part II. In situ straining experiments at low temperature," Acta Materialia, vol. 58, no. 9, pp. 3504–3515, May 2010.

[26] K. Srivastava, R. Gröger, D. Weygand, and P. Gumbsch, "Dislocation motion in tungsten: Atomistic input to discrete dislocation simulations," International Journal of Plasticity, vol. 47, pp. 126–142, Aug. 2013.

[27] J. Friedel, Les Dislocations. Paris: , 1956, p. 314.

[28] M. F. Ashby, "The deformation of plastically non-homogeneous materials," Philosophical Magazine, vol. 21, no. 170, pp. 399–424, Feb. 1970.

[29] H. Mughrabi, "Dislocation wall and cell structures and long-range internal stresses in deformed metal crystals," Acta Metallurgica, vol. 31, no. 9, pp. 1367–1379, Sep. 1983.

[30] I. Aubert and M. Berveiller, "Constrained and unstable expansion of dislocation loops using an invariant formulation of the free energy," Mechanics of Materials, vol. 26, no. 2, pp. 127–137, Sep. 1997.

[31] E. M. Viatkina, W. A. M. Brekelmans, and M. G. D. Geers, "Modelling of the internal stress in dislocation cell structures," European Journal of Mechanics - A/Solids, vol. 26, no. 6, pp. 982–998, Nov. 2007.

[32] E. Rauch, "The Relation Between Forest Dislocations and Stress in BCC Metals," in KEY ENGINEERING MATERIALS, 1994, vol. 97, no. 9, pp. 371–376.

[33] B. Reppich, "Particle strengthening," in Materials Science and Technology: A Comprehensive Treatment. Plastic deformation and fracture of materials., vol. 6, H. Mughrabi, Ed. 1993, p. 19.

[34] S. Queyreau, G. Monnet, and B. Devincre, "Orowan strengthening and forest hardening superposition examined by dislocation dynamics simulations," Acta Materialia, vol. 58, no. 17, pp. 5586–5595, Oct. 2010.

[35] M. S. Duesbery, "The influence of core structure on dislocation mobility," Philosophical Magazine, vol. 19, no. 159, pp. 501–526, Mar. 1969.

[36]   W. A. Spitzig and A. S. Keh, "Orientation dependence of the strain-rate sensitivity and thermally activated flow in iron single crystals," Acta Metallurgica, vol. 18, no. 9, pp. 1021–1033, Sep. 1970.

[37]   W. A. Spitzig, "Analysis of thermally-activated flow in iron single crystals," Acta Metallurgica, vol. 18, no. 12, pp. 1275–1284, Dec. 1970.

[38]   S. Takeuchi, T. Hashimoto, and K. Maeda, "Motion of dislocations in BCC metals at low temperature," in The structure and properties of crystal defects: proceedings of the Symposium on the Structure and Properties of Crystal Defects 1983, 1984, pp. 167–174.

[39]   A. Seeger, "Structure and diffusion of kinks in monatomic crystals," in Colloque International du C.N.R.S. Dislocations, 1984, pp. 141–178.

[40]   A. Couret and D. Caillard, "Dissociations and friction forces in metals and alloys," Journal de Physique III, vol. 1, no. 6, pp. 885–907, Jun. 1991.

[41]   K. Edagawa, T. Suzuki, and S. Takeuchi, "Motion of a screw dislocation in a two-dimensional Peierls potential," Physical Review B, vol. 55, no. 10, pp. 6180–6187, Mar. 1997.

[42]   P. J. Jackson, "The role of cross-slip in the plastic deformation of crystals," Materials Science and Engineering, vol. 57, no. 1, pp. 39–47, Jan. 1983.

[43]   W. Püschl, "Models for dislocation cross-slip in close-packed crystal structures: a critical review," Progress in Materials Science, vol. 47, no. 4, pp. 415–461, Jan. 2002.

[44]   P. Haasen, "Chapter 23 – Mechanical Properties of Solid Solutions," in Physical Metallurgy (Fourth Edition), R. W. Cahn and P. Haasen, Eds. 1996, pp. 2009–2073.

[45]   D. Kuhlmann-Wilsdorf and J. H. Van Der Merwe, "Theory of dislocation cell sizes in deformed metals," Materials Science and Engineering, vol. 55, no. 1, pp. 79–83, Aug. 1982.

[46]   J. Kratochvil, "Dislocation pattern formation in metals," Revue de Physique Appliquée, vol. 23, no. 4, pp. 419–429, 1988.

[47]   P. Hähner, "A theory of dislocation cell formation based on stochastic dislocation dynamics," Acta Materialia, vol. 44, no. 6, pp. 2345–2352, Jun. 1996.